How to cite: *Angew. Chem. Int. Ed.* **2025**, e21397
doi.org/10.1002/anie.202521397

Electrosynthesis | **Very Important Paper**

Synergy of Nickel Single-Atom and Heteroatoms Co-Doping in Carbon for Efficient Hydrogen Peroxide Electrosynthesis

Chunxiao Liu, Kangjuan Cheng, Qiuxu Chen, Zhaoyang Chen, Jinge Wang, Haoyuan Wang, Jialin Tang, Laihao Luo, Xu Li, Tingting Zheng, Qiu Jiang, and Chuan Xia**

Abstract: Single-atom catalysts have emerged as cost-effective alternatives to noble metals for the two-electron oxygen reduction reaction (2e$^-$ ORR); however, their practical application in hydrogen peroxide (H_2O_2) electrosynthesis remains limited by persistent trade-offs among activity, selectivity, and stability. Herein, we demonstrate that synergistic integration of atomically dispersed Ni and B, N co-dopants within a carbon matrix (Ni-BNC) effectively regulates the 2e$^-$ ORR for efficient H_2O_2 production. The Ni-BNC catalyst delivers >90% Faradaic efficiency for H_2O_2 at current densities up to ~−400 mA cm^{-2} and critically maintains this high selectivity for over 50 h at −100 mA cm^{-2} in a flow cell, achieving a maximum production rate of 31.13 mol g^{-1} h^{-1}. In situ infrared spectroscopy and kinetic analysis revealed that B, N-coordination facilitates electron transfer from adjacent single Ni atoms, electronically modulating the *OOH adsorption energy and lowering the kinetic barrier. The practical viability is further demonstrated in a porous solid electrolyte reactor, which continuously produces pure, salt-free H_2O_2 (>1,400 ppm) for 100 h. This work highlights the effectiveness of atomic-level synergy for designing advanced electrocatalysts beyond sole active-site engineering.

Hydrogen peroxide (H_2O_2) stands as a cornerstone chemical in modern industries, with applications ranging from pulp bleaching and semiconductor cleaning to advanced oxidation processes for water treatment.[1,2] Despite its critical role, the conventional anthraquinone process, accounting for >95% of global H_2O_2 production, remains plagued by multistep reactions, high energy consumption (16 GJs per ton of H_2O_2), and reliance on centralized infrastructure that necessitates hazardous transportation of concentrated H_2O_2.[3,4] Electrochemical synthesis of H_2O_2 via the two-electron oxygen reduction reaction (2e$^-$ ORR) offers a promising alternative that could address many of these challenges, potentially allowing for on-site, efficient, and safe H_2O_2 generation.[5] However, to be commercially viable, electrochemical H_2O_2 synthesis must overcome significant hurdles in scalability, necessitating catalysts that provide a delicate balance of high activity, selectivity, and durability under industrially relevant conditions.

Noble-metal catalysts such as Pd-Au and Pt-Hg have shown high 2e$^-$ ORR selectivity (~70–90%) and remain benchmark systems for mechanistic studies and device prototyping.[6–8] However, their cost and stability are problematic for scale: palladium can undergo electrodissolution/dealloying under positive potentials, whereas Hg-containing alloys raise contamination and handling concerns that complicate product purity and environmental compliance.[9–11] In contrast, carbon-based catalysts have emerged as attractive, low-cost candidates. Oxidized carbons/graphenes and defect-engineered carbons have been reported to deliver high H_2O_2 selectivity (>90%) in alkaline media by stabilizing *OOH in the moderate-binding regime.[12–17] However, a crucial limitation persists: many carbon materials exhibit modest intrinsic activity and require substantial extra driving force to attain high current densities (≥100–300 mA cm^{-2}).

To transcend this trade-off, single-atom catalysts (SACs) anchored on carbon matrices have gained traction. SACs maximize metal atom utilization and allow precise electronic/coordination tuning of isolated active centers for the 2e$^-$ ORR.[18–20] Among various metals, Ni-based SACs are especially promising. Representative studies have shown that N-coordinated Ni SACs (Ni-N-C) achieve high H_2O_2 selectivity over broad potential windows and sustain continuous production under alkaline conditions. For example, Shen et al. reported that Ni on N-doped carbon delivered >95% Faradaic efficiency for 100 h of continuous operation;[21] Liang reported that nickel phthalocyanine dispersed on carbon nanotubes exhibited H_2O_2 selectivities of ~83%–92% across 0.70–0.20 V versus a reversible hydrogen electrode (versus RHE).[22] Nevertheless, the symmetric Ni-N_4 motif often binds *OOH slightly too strongly, which promotes the competing 4e$^-$ pathway or facilitates H_2O_2 readsorption/decomposition, yielding sub-optimal H_2O_2 selectivity at industrially relevant current densities.[23–25] Efforts to adjust the local electronic structure by non-nitrogen heteroatoms (e.g., P, O, B) have also shown that these dopants can perturb the Ni coordination environment and

[*] C. Liu, K. Cheng, Q. Chen, Z. Chen, J. Wang, H. Wang, J. Tang, L. Luo, X. Li, T. Zheng, Q. Jiang, C. Xia
School of Materials and Energy, University of Electronic Science and Technology of China, Chengdu 611731, P.R. China
E-mail: jiangqiu@uestc.edu.cn
chuan.xia@uestc.edu.cn

Additional supporting information can be found online in the Supporting Information section

tune adsorption energetics,[26–28] but single-element doping is ultimately constrained by linear scaling relationships.

To overcome these challenges, we posit that tailoring the coordination environment of single Ni atoms through multiheteroatoms synergy could optimize *OOH binding while preserving stability.[29,30] Boron, with its electron-deficient nature and smaller atomic radius than nitrogen does, is uniquely positioned to modulate the electronic structure of adjacent Ni sites. Theory and model studies show that introducing B into N-doped carbon backbones redistributes charge and lowers the metal *d*-band center, weakening *OOH adsorption toward the optimal regime and biasing 2e$^-$ selectivity.[31–33] Guided by this rationale, we engineered a single-atom Ni catalyst embedded in B, N co-doped carbon (Ni-BNC) for efficient 2e$^-$ ORR. Spectroscopic techniques suggest that co-introducing B and N effectively delocalize the electron density around the Ni center, weakening the adsorption energy for *OOH. In the alkaline 2e$^-$ ORR, Ni-BNC reaches an H_2O_2 selectivity of 93% at 0.65 V versus RHE, which is much higher than those of the Ni-N-C and NC controls, while retaining a low overpotential (onset of 0.769 V versus RHE). Furthermore, Ni-BNC exhibits structural resilience, as evidenced by stable operation at -100 mA cm^{-2} for >50 h in a flow cell, with the H_2O_2 Faradaic efficiency remaining above 90%. To validate practical relevance, we integrated Ni-BNC into a solid-state electrolyte (SSE) reactor, circumventing H_2O_2 decomposition and crossover issues inherent to traditional flow cells. The system continuously produces > 1,400 ppm H_2O_2 at 30 mA cm^{-2} for 100 h, achieving a Faraday efficiency of 85%, demonstrating its potential for practical production of high-purity H_2O_2.

Ni-BNC was prepared via a one-pot procedure following our reported protocol.[34] Powder X-ray diffraction (Figure 1a) reveals only broad graphitic (002) and (101) reflections with no detectable peaks from metallic Ni, excluding nanoparticulate Ni in the bulk.[35] Raman spectroscopy (Figure S1) displays the characteristic D and G bands of sp^2 carbon, further confirming a graphitized matrix and the absence of crystalline Ni phases.[36] Scanning electron microscopy (SEM) and transmission electron microscopy (TEM) images (Figure S2a,b) revealed a uniform nanotube-like morphology without visible agglomeration. High-angle annular dark-field scanning TEM (HAADF-STEM) resolves atomically bright, isolated features assigned to individual Ni atoms (Figure 1b,c), with no clusters or nanoparticles observed. Extended X-ray absorption fine structure (EXAFS) spectra of Ni-BNC and Ni-NC presented a main peak at ~1.50 Å attributable to Ni-N/B coordination, while no Ni–Ni bonds (~2.18 Å) were detected, confirming the singly dispersed Ni atoms in both catalysts (Figure 1d).[37] Elemental mapping by energy dispersive X-ray (EDX) demonstrated homogeneous distributions of Ni, B, N, and C across the support (Figure S3). Inductively coupled plasma-atomic emission spectroscopy (ICP-AES) quantifies a Ni content of 0.77 wt % in the Ni-BNC.

The electronic structure was further probed by a suite of spectroscopies. Soft X-ray absorption near-edge structure (NEXAFS) spectra at the N *K*-edge (Figure 1e) exhibit three prominent $1s\rightarrow\pi^*$ resonances attributable to pyridinic N (~397.9 eV), pyrrolic N (~399.3 eV), and graphitic N (~400.9 eV), respectively, in agreement with X-ray photoelectron spectroscopy (XPS) deconvolution.[34,38] In B-containing samples (BNC and Ni-BNC), additional N-environment features, i.e., N = B $1s\rightarrow\pi^*$ (401.8 eV), N = B $1s\rightarrow\sigma^*$ (408.2 eV), and N = C $1s\rightarrow\sigma^*$ (415.9 eV) signals, appear but are absent in NC and Ni-NC (Figure 1e and S4–S7).[34,39] Complementarily, the B *K*-edge spectra (Figure 1f) show well-defined B $1s\rightarrow\pi^*$ transitions consistent with B-C (~190.5 eV) and B-N (~192.0 eV, 192.6 eV, 193.2 eV) motifs, together with B $1s\rightarrow\sigma^*$ bands (~199.6 eV). These fingerprints, which align with those of XPS and Fourier-transform infrared spectroscopy (FTIR) analyses (Figures S4–S9), establish that B and N are co-doped into the carbon lattice and closely interact with one another.[34,40] In particular, upon introducing Ni into the B, N co-doped framework, the B 1*s* and N 1*s* binding energies shift to lower values relative to those of the pristine BNC (Figures S5 and S7 and Tables S1 and S2), indicating increased electron density at the B/N sites and thus a net Ni→(B, N) charge redistribution. Correspondingly, the Ni 2*p* spectrum of Ni-BNC shows a positive shift versus that of Ni-NC (Ni $2p_{3/2}$ at 855.8 eV versus 854.9 eV; Figures S6 and S8 and Table S3), and both are well above that of metallic Ni (852.6 eV)[41,42] in line with the higher-energy absorption edge in the X-ray absorption near-edge structure (XANES) spectrum of the Ni-BNC sample (Figures S10). The conjoint NEXAFS/XPS trends support strong electronic coupling between isolated Ni centers and neighboring B/N dopants within the carbon matrix. Taken together, these results confirm that atomically dispersed Ni sites are embedded in a B, N-coordinated carbon matrix for Ni-BNC. Moreover, the observed electron transfer from Ni increases the electron density at electron-deficient B/N motifs, an effect expected to downshift the Ni *d*-band and reduce the *OOH adsorption strength. This electronic tuning provides a mechanistic basis for the selective 2e$^-$ ORR on Ni-BNC by suppressing O–O scission.

To elucidate how the synergy of Ni SACs and B, N co-dopants steer the two-electron pathway, we benchmarked the intrinsic 2e$^-$ ORR performance of NC, BNC, Ni-NC, and Ni-BNC using rotating ring-disk electrode (RRDE) measurements in 0.1 M KOH under standardized conditions (collection efficiency N = 37%, Figure S11; Pt ring held at 1.25 V versus RHE; 1,600 rpm; 10 mV s^{-1}). Relative to NC and Ni-NC, both B-containing catalysts (BNC and Ni-BNC) display markedly higher ring currents (I_{ring}) across the probed potentials (Figure 2a), directly evidencing enhanced H_2O_2 formation upon B doping. Consistent with this, the calculated electron-transfer numbers approach two (Figure S12), indicating that the 2e$^-$ pathway dominates on BNC and Ni-BNC throughout the relevant potential window. Quantitatively, BNC and Ni-BNC maintain H_2O_2 selectivities exceeding 85% from 0.40 to 0.75 V versus RHE, substantially outperforming NC and Ni-NC (Figure 2b); moreover, Ni-BNC sustains more than 90% selectivity from 0.47 to 0.74 V, highlighting a broadened high-selectivity plateau arising from Ni SACs and B doping. The corresponding Faradaic efficiencies, plotted on the right axis of Figure 2b, follow the same trend. We further

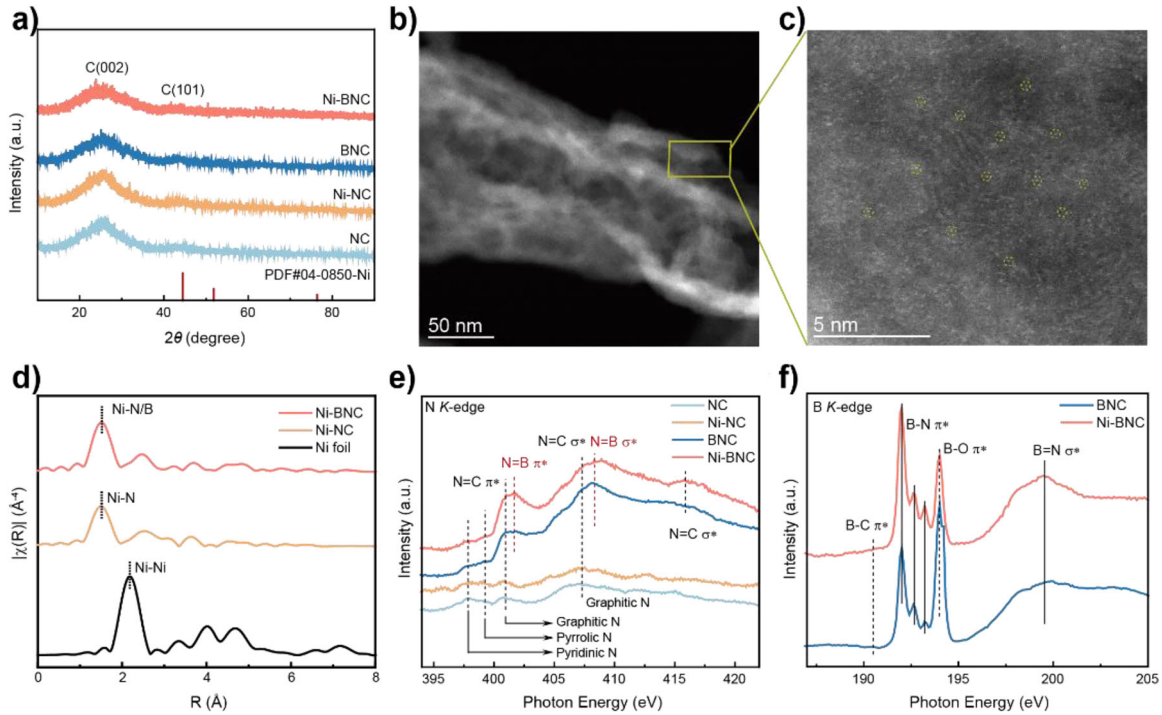

Figure 1. Characterization of the catalysts. a) XRD patterns of the NC catalysts. b) HAADF-STEM image of a Ni-BNC. c) Localized enlargement of (b). d) Ni *K*-edge EXAFS spectra of Ni-BNC, Ni-NC, and Ni foil. e) N *K*-edge NEXAFS of NC catalysts. f) B *K*-edge NEXAFS spectra of BNC and Ni-BNC.

compared kinetics via the onset potential, defined here as the potential at which the ring current density reaches 0.1 mA cm^{-2} from the RRDE polarization curves. Ni-BNC exhibits the most positive onset potential (0.769 V), followed by BNC (0.751 V), Ni-NC (0.720 V), and NC (0.716 V) (Figure 2c). The lower onset potential indicated accelerated $2e^-$ ORR kinetics due to synergistic Ni and B, N co-doping. Of note, the onset potentials reported in this work are more positive than the thermodynamic theoretical potentials (0.7 V versus RHE) because of the Nernst-related potential shift caused by local pH changes.[40,43,44] Collectively, the RRDE results confirm that the strategic immobilization of Ni SACs on B, N co-doped carbon significantly enhances both the selectivity and reaction kinetics of the $2e^-$ ORR pathway.

While RRDE tests indicated enhanced $2e^-$ ORR catalytic performance through strategic co-doping, the catalysts operate under oxygen-transport limitations inherent to aqueous electrolytes (low O_2 solubility and diffusivity) and therefore offer limited guidance for practical production. We thus assessed the catalytic behavior in a gas-diffusion flow cell. By establishing a triple-phase gas-liquid-solid interface at the gas-diffusion electrode (GDE), oxygen mass-transfer constraints are alleviated, enabling evaluation at high current densities. Electrolysis was performed galvanostatically. The produced H_2O_2 was quantified using a colorimetric method with $Ti(SO_4)_2$ after acidification, followed by analysis via ultraviolet–visible (UV–vis) spectroscopy (Figures S13 and S14). The polarization curves (Figure 3a) reveal that, compared with the other samples, Ni-BNC exhibits superior H_2O_2 production activity, as evidenced by a significantly lower overpotential, particularly at high current densities. In terms of selectivity, Ni-BNC maintained Faradaic efficiencies (FEs) for H_2O_2 exceeding 90% across a current density range of -100 to -400 mA cm^{-2}. In contrast, the H_2O_2 FEs for BNC were 10%–20% lower, and both B doped catalysts significantly outperformed Ni-NC and NC (Figure 3b), which is consistent with the RRDE trends. Notably, Ni-BNC achieved a peak H_2O_2 FE of 95.7% at -100 mA cm^{-2}, corresponding to a production rate of 7.14 mol g_{cat}^{-1} h^{-1} (1.79 mmol cm^{-2} h^{-1}). Even at a high current density of -500 mA cm^{-2}, the catalyst sustained an H_2O_2 FE of 83.4% at an applied potential of just 0.58 V versus RHE. This performance equates to an H_2O_2 partial current density of -417 mA cm^{-2} and a production rate of 31.13 mol g_{cat}^{-1} h^{-1} (7.78 mmol cm^{-2} h^{-1}, Figures S15 and S16). Benchmarking against recent reports indicates that this production rate at high current densities compares favorably with the state-of-the-art catalysts in flow-cell electrosynthesis (Figure 3c and S17 and Table S4). To evaluate the intrinsic catalytic activity, the H_2O_2 partial current density (jH_2O_2) was normalized to the electrochemically active surface area (ECSA). The results confirm that Ni-BNC possesses a higher intrinsic activity than the control catalysts do, further underscoring the synergistic enhancement conferred by Ni and B, N co-doping (Figures S18 and 3d). Durability is also critical for continuous, decentralized H_2O_2 generation. We therefore conducted a prolonged electrolysis test for Ni-BNC at a constant current density of −100 mA cm^{-2}. The catalyst maintained steady operation for >50 h with H_2O_2 FE consistently above 90% (Figures 3e and S19). Furthermore, post-reaction characterizations were conducted to confirm the structural stability of catalytic sites, excluding the Ni leaching and the formation of Ni particles or aggregates (Figures S20–S22

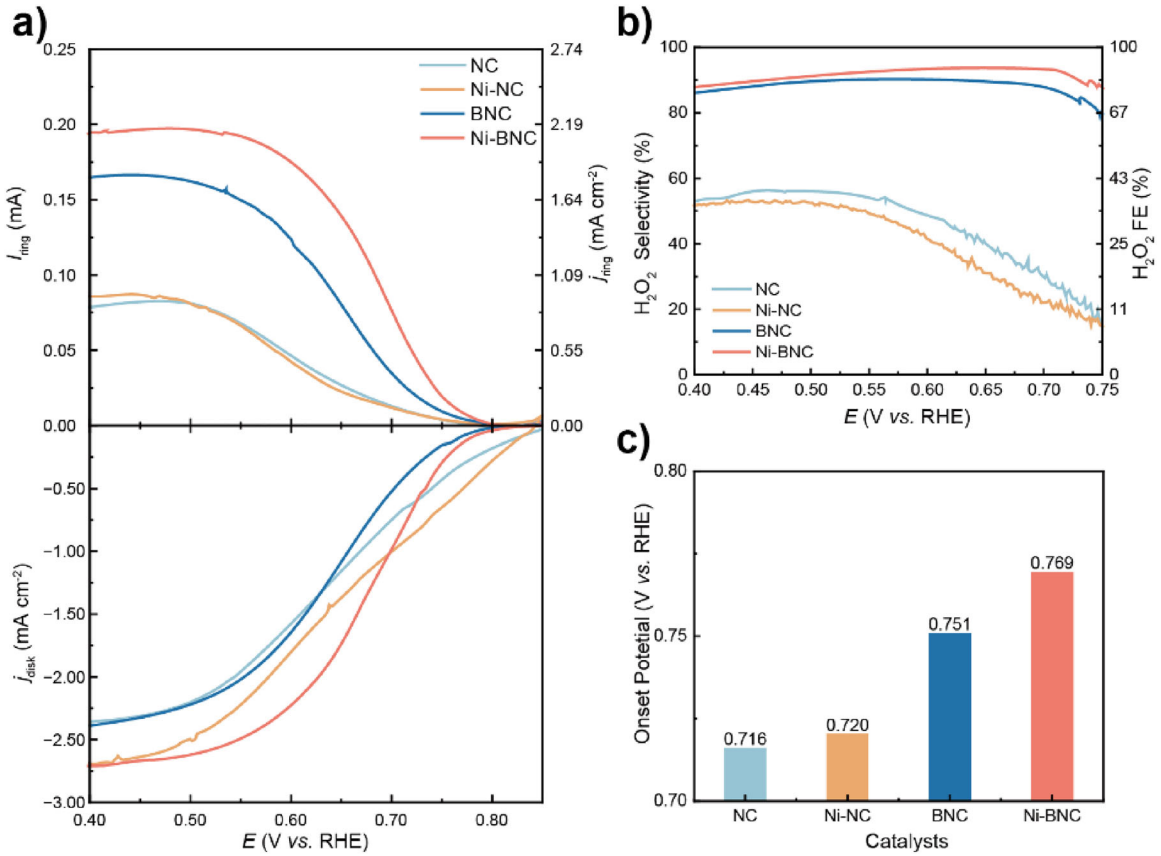

Figure 2. 2e$^-$ ORR performance evaluation by RRDE in 0.1 M KOH. a) Polarized curves of NC-based catalysts recorded with a rotation rate of 1,600 rpm and a scan rate of 10 mV s^{-1}, together with the detected H_2O_2 currents on the Pt ring electrode at a fixed potential of 1.25 V versus RHE. b) The corresponding H_2O_2 selectivity (left axis) and FE (right axis). c) Onset potentials (j_{ring}@0.1 mA cm^{-2}) of different catalysts.

and Table S5). Taken together, the high-rate activity, broad high-FE window, and long-duration stability make Ni-BNC a strong candidate for scalable H_2O_2 electrosynthesis.

To identify the catalytically active sites and clarify the reaction pathway, we combined kinetic analysis with in situ infrared spectroscopy. Tafel analysis (Figure 4a) revealed distinct kinetic profiles for these samples. NC and Ni-NC exhibited sluggish kinetics with Tafel slopes close to 150 mV dec^{-1}, suggesting a rate-determining step (RDS) involving the first electron transfer to form the *OOH intermediate ($O_2 + * + H^+ + e^- \rightarrow$ *OOH).[31,45] In contrast, BNC and Ni-BNC demonstrated significantly enhanced kinetics, with Tafel slopes of 88 and 69 mV dec^{-1}, respectively, which is consistent with an RDS of H_2O_2 formation (*OOH + $H^+ + e^- \rightarrow H_2O_2$). This result indicated that B, N coordination shifts the rate-determining step toward H_2O_2 formation.[39,46] Notably, the Tafel slopes of BNC and Ni-BNC are close, suggesting a shared pathway; however, Ni-BNC (69 mV dec^{-1}) is lower than BNC (88 mV dec^{-1}), indicating that introducing Ni SACs further accelerates the interfacial charge-transfer kinetics. Moreover, we have conducted electrochemical impedance spectroscopy (EIS) measurements. As shown in Figure S23, the Nyquist plots reveal that Ni-BNC exhibits the smallest charge-transfer resistance, indicating faster electron transfer kinetics and enhanced 2e$^-$ ORR activity, consistent with Tafel results. To probe the specific role of the Ni SACs, we performed site poisoning by introducing 10 mM thiocyanate (SCN^-) into 0.1 M KOH. As shown in Figure 4b, the ORR current density decreases and the overpotential increases upon SCN^- addition, consistent with the coordination of SCN^- to Ni centers and the consequent suppression of their contribution.[47] This observation suggested that Ni sites participate directly in and promote the 2e$^-$ ORR due to their oxygenophilic nature.[48] Further insight was obtained by in situ electrochemical attenuated total reflection surface-enhanced infrared absorption spectroscopy (ATR-SEIRAS). Both BNC and Ni-BNC display vibrational signatures assignable to *OOH at similar adsorption geometries (Figure 4c).[49] Importantly, the *OOH-related band for Ni-BNC appears at 1212 cm^{-1}, which is slightly blueshifted relative to that of BNC (1209 cm^{-1}). This shift to a higher wavenumber indicates weaker *OOH binding on Ni-BNC, aligning with the electronic picture of charge redistribution and the selectivity trends. Taken together, these studies support a mechanism in which the oxygenophilic Ni center withdraws electron density from adjacent B and N atoms, weakening the adsorption strength of *OOH. This optimized adsorption energy lowers the kinetic barrier for H_2O_2 desorption, accounting for the enhanced activity and selectivity of Ni-BNC.

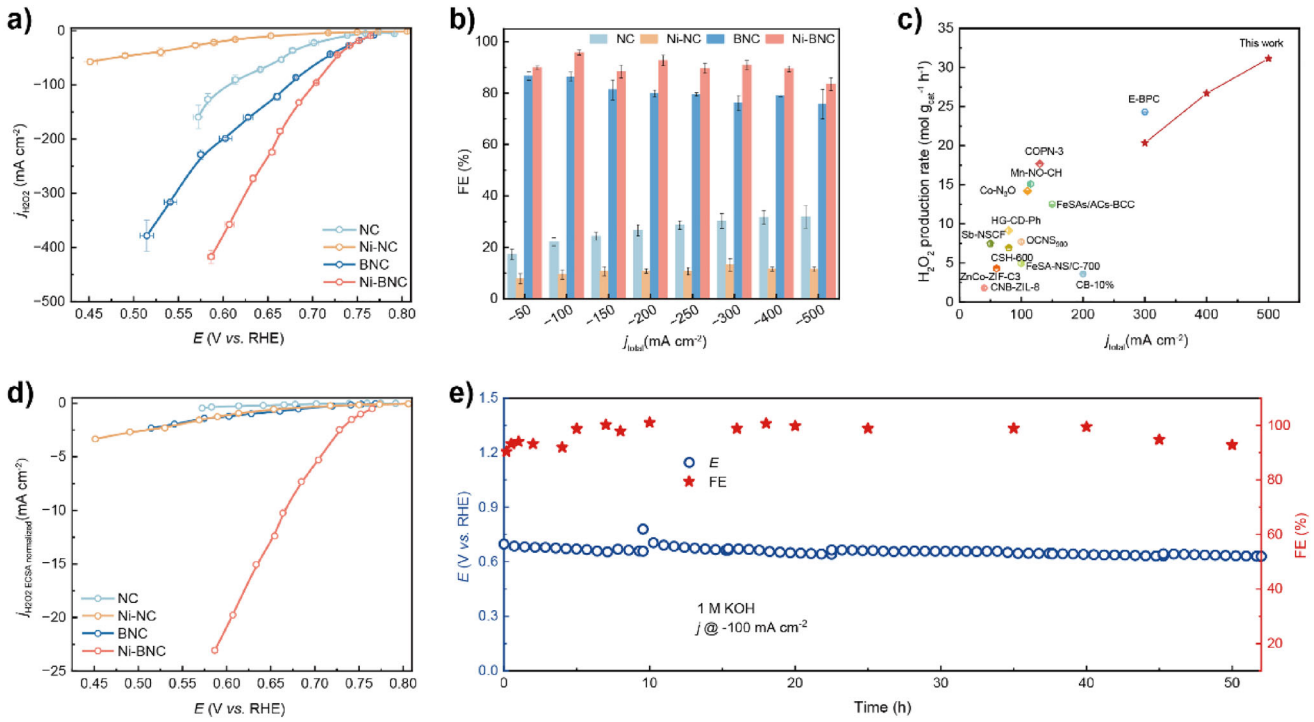

Figure 3. 2e⁻ ORR performance of different catalysts in a flow cell using 1 M KOH. a) H_2O_2 partial current density j_{H2O2}. b) FE of H_2O_2 at different current densities. c) Benchmark of H_2O_2 production rates from reported electrocatalysts in a flow cell. d) j_{H2O2} normalized by the ECSA. e) Stability of the BNC in 1 M KOH at −100 mA cm^{-2}.

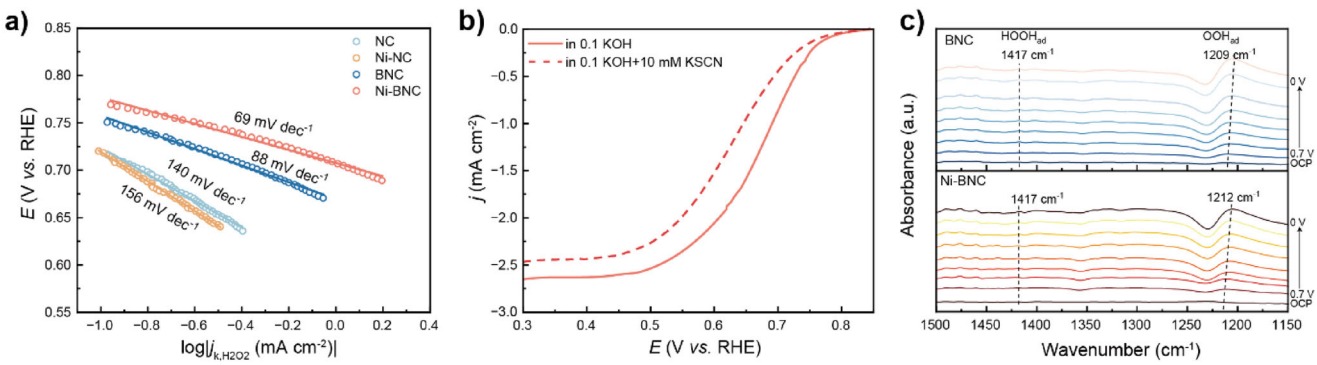

Figure 4. Mechanism study of the 2e⁻ ORR catalysts. a) Tafel slopes of different catalysts. b) Toxic chemical experiments on Ni-BNC. Adding 10 mM KSCN to 0.1 M KOH to poison Ni single atom using SCN^-. c) In situ ATR-SEIRAS spectra of Ni-BNC and BNC catalysts under various potentials, respectively.

Conventional H-cells and liquid-electrolyte flow cells co-generate H_2O_2 with supporting salts (e.g., KOH or H_2SO_4), necessitating costly downstream separation.[12,43,50,51] To circumvent this constraint, we employed a porous solid electrolyte (PSE) architecture in which deionized (DI) water is circulated through an intermediate solid-electrolyte layer to strip the product directly as an electrolyte-free H_2O_2 solution; the outlet concentration is readily tuned by adjusting the DI-water flow rate.[13,31,52] The PSE reactor is built as a layered stack (Figure 5a): an IrO_2 anode and proton-exchange membrane (PEM) on the anode side, a porous solid-state electrolyte (SSE) layer in the middle, and a Ni-BNC cathode with an anion-exchange membrane (AEM) on the cathode side. During operation, the anode generates protons (H^+), which migrate through the PEM into the SSE layer, while the cathode produces HO_2^-, which crosses the AEM into the same layer. These two ionic fluxes meet and recombine in the SSE layer to form H_2O_2 in situ, which is then collected directly by flowing deionized water through the middle layer. Under galvanostatic operation from 10 to 500 mA cm^{-2}, the cell sustains FE of H_2O_2 > 70% across the entire range; at 30 mA cm^{-2}, FE of H_2O_2 peaks at 97%; at 500 mA cm^{-2}, the H_2O_2 production rate reaches 6.79 mmol cm^{-2} h^{-1} at a cell voltage < 4.5 V (Figure 5b,c). The system also demonstrates robust durability. Ni-BNC maintained an H_2O_2 FE above 80% at 30 mA cm^{-2} for over 100 h (Figure 5d)

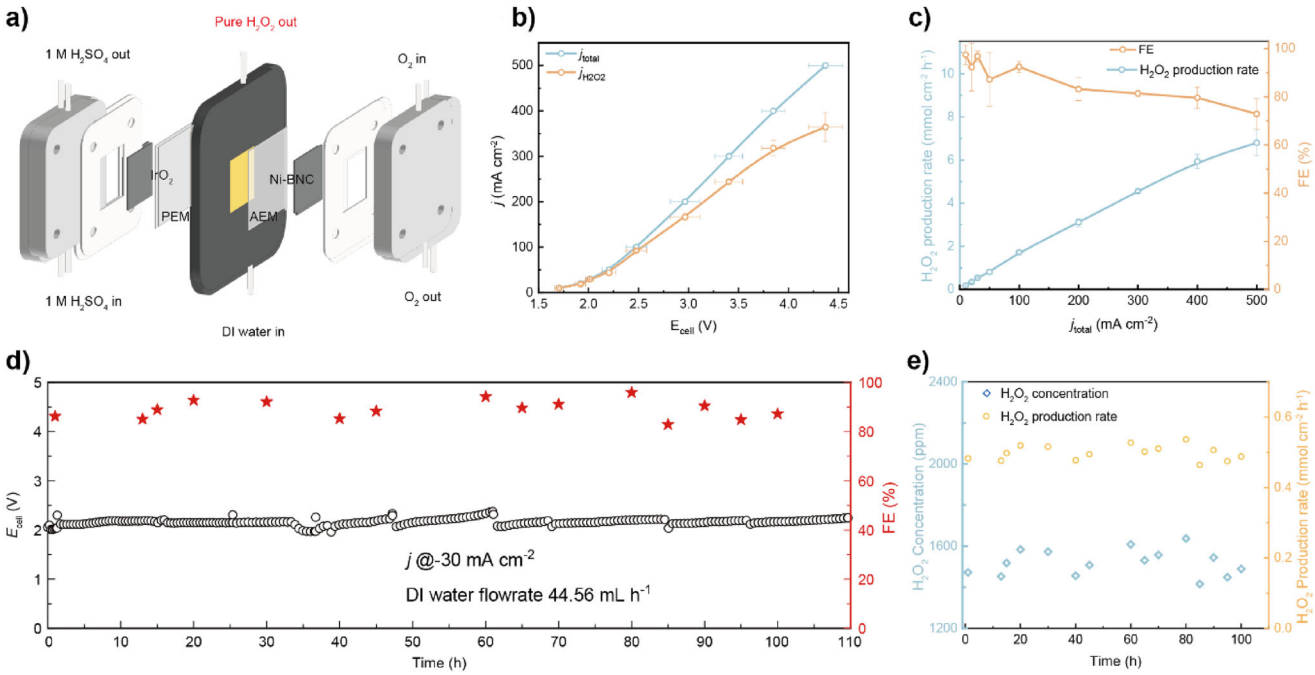

Figure 5. Practical synthesis of pure H_2O_2 in an SSE reactor. a) Schematic illustration of the SSE structure diagram. b) *j*–V curves and H_2O_2 partial current density. c) Corresponding H_2O_2 FE and production rate. d) Stability of Ni-BNC in the PSE at 30 mA cm^{-2}. e) Corresponding H_2O_2 concentration and production rate.

while delivering an outlet concentration > 1,400 ppm and a production rate > 0.46 mmol cm^{-2} h^{-1} during the stability run (Figure 5e). Taken together, the integration of Ni-BNC with a PSE reactor enables salt-free peroxide generation with high efficiency, tunable concentrations, and long-term stable operation. To benchmark this against the incumbent anthraquinone process, we conducted a preliminary techno-economic analysis (Figure S24). The estimated cost for on-site H_2O_2 production is as low as 0.21 USD kg_{H2O2}^{-1}, which is lower than the ~1.20 USD kg_{H2O2}^{-1} cost associated with the conventional process.

In conclusion, we developed a Ni-BNC catalyst featuring atomically dispersed Ni sites within a B, N co-doped carbon framework for highly selective 2e$^-$ ORR. The catalyst delivered > 90% H_2O_2 selectivity within a broad potential window of 0.47–0.74 V versus RHE and an onset potential of 0.769 V in RRDE measurements. When evaluated in a flow cell configuration, Ni-BNC maintains Faradaic efficiencies exceeding 90% across current densities from −100 to −400 mA cm^{-2} and show remarkable stability, sustaining > 90% FE over 50 h of continuous operation at −100 mA cm^{-2}, corresponding to a production rate of 31.13 mol g_{cat}^{-1} h^{-1}. Mechanistic studies indicate that introducing B, N coordination redistributes charges around Ni SACs, weakening *OOH adsorption, which favors H_2O_2 formation. When implemented in a PSE reactor, the catalyst enables continuous production of salt-free H_2O_2 at concentrations exceeding 1,400 ppm for 100 h at 30 mA cm^{-2}. This work establishes an effective strategy for tuning electrochemical reaction pathways through atomic-level coordination design.

Acknowledgements

The authors acknowledge the National Key Research and Development Program of China (2024YFB4105700), the National Natural Science Foundation of China (22322201, 52171201, 22278067, 22308050, 22301031), and the Natural Science Foundation of Sichuan Province (2025NSFJQ0017, 2024NSFSC1104, 2024NSFSC0953). The authors appreciate the Analysis and Testing Center, University of Electronic Science and Technology of China, for their technical support.

Conflict of Interests

A China provisional patent application (ZL202510210554.2) based on the technology described in this work was filed in February 2025 by T.Z., K.C., C.X., X.L., and Q.J. at the University of Electronic Science and Technology of China. The remaining authors declare no conflict of interest.

Data Availability Statement

The data that support the findings of this study are available from the corresponding author upon reasonable request.

Keywords: 2e$^-$ O_2 electroreduction · H_2O_2 electrosynthesis · Multicomponent doping · Ni single atom · Porous solid electrolyte reactor

[1] E. Brillas, I. Sirés, M. A. Oturan, *Chem. Rev.* **2009**, *109*, 6570–6631, https://doi.org/10.1021/cr900136g.

[2] J.-Y. Zhang, C. Xia, H.-F. Wang, C. Tang, *J. Energy Chem.* **2022**, *67*, 432–450, https://doi.org/10.1016/j.jechem.2021.10.013.

[3] J. S. J. Hargreaves, Y.-M. Chung, W.-S. Ahn, T. Hisatomi, K. Domen, M. C. Kung, H. H. Kung, *Appl. Catal. A: Gen.* **2020**, *594*, 117419, https://doi.org/10.1016/j.apcata.2020.117419.

[4] J. M. Campos-Martin, G. Blanco-Brieva, J. L. G. Fierro, *Angew. Chem. Int. Ed.* **2006**, *45*, 6962–6984, https://doi.org/10.1002/anie.200503779.

[5] E. Berl, *Trans. Electrochem. Soc.* **1939**, *76*, 359–369, https://doi.org/10.1149/1.3500291.

[6] E. Pizzutilo, O. Kasian, C. H. Choi, S. Cherevko, G. J. Hutchings, K. J. J. Mayrhofer, S. J. Freakley, *Chem. Phys. Lett.* **2017**, *683*, 436–442, https://doi.org/10.1016/j.cplett.2017.01.071.

[7] X. Zhao, H. Yang, J. Xu, T. Cheng, Y. Li, *ACS Mater. Lett.* **2021**, *3*, 996–1002, https://doi.org/10.1021/acsmaterialslett.1c00263.

[8] N. Wang, S. Ma, P. Zuo, J. Duan, B. Hou, *Adv. Sci.* **2021**, *8*, 2100076, https://doi.org/10.1002/advs.202100076.

[9] K. Hubkowska, J. Kubisztal, M. Pająk, B. Łosiewicz, A. Czerwiński, *Materials* **2021**, *14*, 2923, https://doi.org/10.3390/ma14112923.

[10] E. Pizzutilo, S. Geiger, S. J. Freakley, A. Mingers, S. Cherevko, G. J. Hutchings, K. J. J. Mayrhofer, *Electrochim. Acta* **2017**, *229*, 467–477, https://doi.org/10.1016/j.electacta.2017.01.127.

[11] A. Chalkidis, D. Jampaiah, A. Aryana, C. D. Wood, P. G. Hartley, Y. M. Sabri, S. K. Bhargava, *J. Environ. Manage.* **2020**, *270*, 110945, https://doi.org/10.1016/j.jenvman.2020.110945.

[12] Z. Lu, G. Chen, S. Siahrostami, Z. Chen, K. Liu, J. Xie, L. Liao, T. Wu, D. Lin, Y. Liu, T. F. Jaramillo, J. K. Nørskov, Y. Cui, *Nat. Catal.* **2018**, *1*, 156–162, https://doi.org/10.1038/s41929-017-0017-x.

[13] C. Xia, Y. Xia, P. Zhu, L. Fan, H. Wang, *Science* **2019**, *366*, 226–231, https://doi.org/10.1126/science.aay1844.

[14] J. An, Y. Feng, Q. Zhao, X. Wang, J. Liu, N. Li, *Environ. Sci. Ecotechnol.* **2022**, *11*, 100170, https://doi.org/10.1016/j.ese.2022.100170.

[15] Q. Wu, H. Zou, X. Mao, J. He, Y. Shi, S. Chen, X. Yan, L. Wu, C. Lang, B. Zhang, L. Song, X. Wang, A. Du, Q. Li, Y. Jia, J. Chen, X. Yao, *Nat. Commun.* **2023**, *14*, 6275, https://doi.org/10.1038/s41467-023-41947-7.

[16] J. Su, L. Jiang, B. Xiao, Z. Liu, H. Wang, Y. Zhu, J. Wang, X. Zhu, *Small* **2023**, *20*, 2310317.

[17] G.-F. Han, F. Li, W. Zou, M. Karamad, J.-P. Jeon, S.-W. Kim, S.-J. Kim, Y. Bu, Z. Fu, Y. Lu, S. Siahrostami, J.-B. Baek, *Nat. Commun.* **2020**, *11*, 2209, https://doi.org/10.1038/s41467-020-15782-z.

[18] H. Xu, S. Zhang, H. Zhang, *ChemElectroChem* **2024**, *11*, e202300630.

[19] X. Gao, G. Huang, S. Jing, S. Xu, Z. Z. Xue, L. Wang, N. Li, *Innov. Mater.* **2025**, *3*, 100141, https://doi.org/10.59717/j.xinnmater.2025.100141.

[20] H. Yin, R. Pan, M. Zou, X. Ge, C. Shi, J. Yuan, C. Huang, H. Xie, *Nanomaterials* **2024**, *14*, 835, https://doi.org/10.3390/nano14100835.

[21] H. Shen, L. Pan, T. Thomas, J. Wang, X. Guo, Y. Zhu, K. Luo, S. Du, H. Guo, G. J. Hutchings, J. P. Attfield, M. Yang, *Cell Rep. Phys. Sci.* **2020**, *1*, 100255, https://doi.org/10.1016/j.xcrp.2020.100255.

[22] Y. Wang, Z. Zhang, X. Zhang, Y. Yuan, Z. Jiang, H. Zheng, Y.-G. Wang, H. Zhou, Y. Liang, *CCS Chem* **2021**, *3*, 585.

[23] X. Li, W. Xu, L. Q. Le, S. Chen, L. Song, T. S. Choksi, X. Wang, *Chem. Catal.* **2023**, *3*, 100724.

[24] C. Tang, L. Chen, H. Li, L. Li, Y. Jiao, Y. Zheng, H. Xu, K. Davey, S.-Z. Qiao, *J. Am. Chem. Soc.* **2021**, *143*, 7819–7827, https://doi.org/10.1021/jacs.1c03135.

[25] Y. Wang, R. Shi, L. Shang, G. I. N. Waterhouse, J. Zhao, Q. Zhang, L. Gu, T. Zhang, *Angew. Chem. Int. Ed.* **2020**, *59*, 13057–13062, https://doi.org/10.1002/anie.202004841.

[26] Z. Zhou, Y. Kong, H. Tan, Q. Huang, C. Wang, Z. Pei, H. Wang, Y. Liu, Y. Wang, S. Li, X. Liao, W. Yan, S. Zhao, *Adv. Mater.* **2022**, *34*, 2106541, https://doi.org/10.1002/adma.202106541.

[27] Z. Wu, T. Wang, J.-J. Zou, Y. Li, C. Zhang, *ACS Catal.* **2022**, *12*, 5911–5920, https://doi.org/10.1021/acscatal.2c01829.

[28] J. Wu, M. Hou, Z. Chen, W. Hao, X. Pan, H. Yang, W. Cen, Y. Liu, H. Huang, P. W. Menezes, Z. Kang, *Adv. Mater.* **2022**, *34*, 2202995, https://doi.org/10.1002/adma.202202995.

[29] C. Xiao, L. Cheng, Y. Zhu, G. Wang, L. Chen, Y. Wang, R. Chen, Y. Li, C. Li, *Angew. Chem. Int. Ed.* **2022**, *61*, e202206544, https://doi.org/10.1002/anie.202206544.

[30] W. Liu, R. Chen, Z. Sang, Z. Li, J. Nie, L. Yin, F. Hou, J. Liang, *Adv. Mater.* **2024**, *36*, 2406403, https://doi.org/10.1002/adma.202406403.

[31] Y. Xia, X. Zhao, C. Xia, Z.-Y. Wu, P. Zhu, J. Y. Kim, X. Bai, G. Gao, Y. Hu, J. Zhong, Y. Liu, H. Wang, *Nat. Commun.* **2021**, *12*, 4225.

[32] N. Cao, N. Zhang, K. Wang, K. Yan, P. Xie, *Chem. Synth.* **2023**, *3*, 23, https://doi.org/10.20517/cs.2023.09.

[33] H. Sun, M. Wang, X. Du, Y. Jiao, S. Liu, T. Qian, Y. Yan, C. Liu, M. Liao, Q. Zhang, L. Meng, L. Gu, J. Xiong, C. Yan, *J. Mater. Chem. A* **2019**, *7*, 20952–20957, https://doi.org/10.1039/C9TA06949F.

[34] X. Zhang, P. Yan, J. Xu, F. Li, F. Herold, B. J. M. Etzold, P. Wang, D. S. Su, S. Lin, W. Qi, Z. Xie, *Sci. Adv.* **2020**, *6*, eaba5778.

[35] Z. Q. Li, C. J. Lu, Z. P. Xia, Y. Zhou, Z. Luo, *Carbon* **2007**, *45*, 1686.

[36] R. Yuan, Y. Guo, I. Gurgan, N. Siddique, Y.-S. Li, S. Jang, G. A. Noh, S. H. Kim, *Carbon* **2025**, *238*, 120214, https://doi.org/10.1016/j.carbon.2025.120214.

[37] Y. Kong, X. Jia, X. Chai, Z. Chen, C. Shang, X. Jiang, H. Cai, L. Jing, Q. Hu, H. Yang, X. Zhang, C. He, *Natl. Sci. Rev.* **2025**, *12*, nwaf173, https://doi.org/10.1093/nsr/nwaf173.

[38] B. Ni, P. Shen, G. Zhang, J. Zhao, H. Ding, Y. Ye, Z. Yue, H. Yang, H. Wei, K. Jiang, *J. Am. Chem. Soc.* **2024**, *146*, 11181.

[39] Y. Dai, H. Li, C. Wang, W. Xue, M. Zhang, D. Zhao, J. Xue, J. Li, L. Luo, C. Liu, X. Li, P. Cui, Q. Jiang, T. Zheng, S. Gu, Y. Zhang, J. Xiao, C. Xia, J. Zeng, *Nat. Commun.* **2023**, *14*, 3382, https://doi.org/10.1038/s41467-023-39048-6.

[40] S. Chen, Z. Chen, S. Siahrostami, D. Higgins, D. Nordlund, D. Sokaras, T. R. Kim, Y. Liu, X. Yan, E. Nilsson, R. Sinclair, J. K. Nørskov, T. F. Jaramillo, Z. Bao, *J. Am. Chem. Soc.* **2018**, *140*, 7851–7859, https://doi.org/10.1021/jacs.8b02798.

[41] T. Zheng, K. Jiang, N. Ta, Y. Hu, J. Zeng, J. Liu, H. Wang, *Joule* **2019**, *3*, 265–278, https://doi.org/10.1016/j.joule.2018.10.015.

[42] R. Yao, K. Sun, K. Zhang, Y. Wu, Y. Du, Q. Zhao, G. Liu, C. Chen, Y. Sun, J. Li, *Nat. Commun.* **2024**, *15*, 2218, https://doi.org/10.1038/s41467-024-46553-9.

[43] S. Siahrostami, A. Verdaguer-Casadevall, M. Karamad, D. Deiana, P. Malacrida, B. Wickman, M. Escudero-Escribano, E. A. Paoli, R. Frydendal, T. W. Hansen, I. Chorkendorff, I. E. L. Stephens, J. Rossmeisl, *Nat. Mater.* **2013**, *12*, 1137–1143, https://doi.org/10.1038/nmat3795.

[44] E. Jung, H. Shin, B.-H. Lee, V. Efremov, S. Lee, H. S. Lee, J. Kim, W. Hooch Antink, S. Park, K.-S. Lee, S.-P. Cho, J. S. Yoo, Y.-E. Sung, T. Hyeon, *Nat. Mater.* **2020**, *19*, 436–442, https://doi.org/10.1038/s41563-019-0571-5.

[45] A. Holewinski, S. Linic, *J. Electrochem. Soc.* **2012**, *159*, H864–H870, https://doi.org/10.1149/2.022211jes.

[46] M. Fan, Z. Wang, K. Sun, A. Wang, Y. Zhao, Q. Yuan, R. Wang, J. Raj, J. Wu, J. Jiang, L. Wang, *Adv. Mater.* **2023**, *35*, 2209086, https://doi.org/10.1002/adma.202209086.
[47] Y. Sun, K. Fan, J. Li, L. Wang, Y. Yang, Z. Li, M. Shao, X. Duan, *Nat. Commun.* **2024**, *15*, 6098, https://doi.org/10.1038/s41467-024-50446-2.
[48] Z. Liu, W. Yuan, H. Yang, Z. Kang, M. Ma, P. W. Menezes, Z. Chen, *Adv. Funct. Mater.* **2025**, *35*, 2412198, https://doi.org/10.1002/adfm.202412198.
[49] S. Chen, T. Luo, X. Li, K. Chen, J. Fu, K. Liu, C. Cai, Q. Wang, H. Li, Y. Chen, C. Ma, L. Zhu, Y.-R. Lu, T.-S. Chan, M. Zhu, E. Cortés, M. Liu, *J. Am. Chem. Soc.* **2022**, *144*, 14505–14516, https://doi.org/10.1021/jacs.2c01194.
[50] B.-H. Lee, H. Shin, A. S. Rasouli, H. Choubisa, P. Ou, R. Dorakhan, I. Grigioni, G. Lee, E. Shirzadi, R. K. Miao, J. Wicks, S. Park, H. S. Lee, J. Zhang, Y. Chen, Z. Chen, D. Sinton, T. Hyeon, Y.-E. Sung, E. H. Sargent, *Nat. Catal.* **2023**, *6*, 234–243, https://doi.org/10.1038/s41929-023-00924-5.
[51] S. C. Perry, D. Pangotra, L. Vieira, L.-I. Csepei, V. Sieber, L. Wang, C. Ponce De León, F. C. Walsh, *Nat. Rev. Chem.* **2019**, *3*, 442–458, https://doi.org/10.1038/s41570-019-0110-6.
[52] X. Zhang, X. Zhao, P. Zhu, Z. Adler, Z.-Y. Wu, Y. Liu, H. Wang, *Nat. Commun.* **2022**, *13*, 2880, https://doi.org/10.1038/s41467-022-30337-0.

Manuscript received: September 30, 2025
Revised manuscript received: October 28, 2025
Manuscript accepted: December 05, 2025
Version of record online: ■■, ■■